

University of Dundee

## Experimental and numerical studies on internal solitary waves with a free surface

Zhao, B. B.; Wang, Z.; Duan, W. Y.; Cengiz Ertekin, R.; Hayatdavoodi, M.; Zhang, T. Y .

*Published in:*  
Journal of Fluid Mechanics

*DOI:*  
[10.1017/jfm.2020.451](https://doi.org/10.1017/jfm.2020.451)

*Publication date:*  
2020

*Document Version*  
Peer reviewed version

[Link to publication in Discovery Research Portal](#)

*Citation for published version (APA):*  
Zhao, B. B., Wang, Z., Duan, W. Y., Cengiz Ertekin, R., Hayatdavoodi, M., & Zhang, T. Y . (2020). Experimental and numerical studies on internal solitary waves with a free surface. *Journal of Fluid Mechanics*, 899, [A17].  
<https://doi.org/10.1017/jfm.2020.451>

### General rights

Copyright and moral rights for the publications made accessible in Discovery Research Portal are retained by the authors and/or other copyright owners and it is a condition of accessing publications that users recognise and abide by the legal requirements associated with these rights.

- Users may download and print one copy of any publication from Discovery Research Portal for the purpose of private study or research.
- You may not further distribute the material or use it for any profit-making activity or commercial gain.
- You may freely distribute the URL identifying the publication in the public portal.

### Take down policy

If you believe that this document breaches copyright please contact us providing details, and we will remove access to the work immediately and investigate your claim.

University of Dundee

## Experimental and numerical studies on internal solitary waves with a free surface

Zhao, B. B.; Wang, Z.; Duan, W. Y.; Cengiz Ertekin, R.; Hayatdavoodi, M.; Zhang, T Y

*Published in:*  
Journal of Fluid Mechanics

*Publication date:*  
2020

*Document Version*  
Peer reviewed version

[Link to publication in Discovery Research Portal](#)

### *Citation for published version (APA):*

Zhao, B. B., Wang, Z., Duan, W. Y., Cengiz Ertekin, R., Hayatdavoodi, M., & Zhang, T. Y. (Accepted/In press). Experimental and numerical studies on internal solitary waves with a free surface. *Journal of Fluid Mechanics*. v.899: A17 pp. 1-28, published online 21 July 2020. Available <https://doi.org/10.1017/jfm.2020.451>

### General rights

Copyright and moral rights for the publications made accessible in Discovery Research Portal are retained by the authors and/or other copyright owners and it is a condition of accessing publications that users recognise and abide by the legal requirements associated with these rights.

- Users may download and print one copy of any publication from Discovery Research Portal for the purpose of private study or research.
- You may not further distribute the material or use it for any profit-making activity or commercial gain.
- You may freely distribute the URL identifying the publication in the public portal.

### Take down policy

If you believe that this document breaches copyright please contact us providing details, and we will remove access to the work immediately and investigate your claim.

# Experimental and numerical studies on internal solitary waves with a free surface

B. B. Zhao<sup>1</sup>, Z. Wang<sup>1,†</sup>, W. Y. Duan<sup>1</sup>, R. C. Ertekin<sup>2,1</sup>, M. Hayatdavoodi<sup>3,1</sup> and T. Y. Zhang<sup>1</sup>

<sup>1</sup>College of Shipbuilding Engineering, Harbin Engineering University, 150001 Harbin, China

<sup>2</sup>Department of Ocean & Resources Engineering, University of Hawai'i, Honolulu, HI 96822, USA

<sup>3</sup>Civil Engineering Department, School of Science and Engineering, University of Dundee, Dundee DD1 4HN, UK

(Received xx; revised xx; accepted xx)

Large-amplitude internal solitary waves in a two-layer fluid system with a free surface are investigated in this paper. Experiments on strongly nonlinear internal solitary waves with a free surface for a deep configuration are conducted. After comparing the experimental data with the results of the model derived by Miyata, Choi & Camassa that includes the free-surface effects (MCC-FS model), we find that the MCC-FS model does not calculate accurately the internal solitary waves with a free surface. Thus, we develop a strongly nonlinear model for a deep configuration, namely the two-layer High-Level Green-Naghdi model that includes the free-surface effects (HLGN-FS model). Numerical results of the HLGN-FS model, including the wave profile, velocity field and wave speed, are presented for three cases. The first case is a shallow configuration with  $\rho_2/\rho_1 = 0.977$  and  $h_2/h_1 = 1/4.13$ , where  $\rho_2$  and  $\rho_1$  are the densities of the upper-fluid layer and the lower-fluid layer, respectively, and  $h_2$  and  $h_1$  are the depths of the upper-fluid layer and the lower-fluid layer, respectively. The second case is also a shallow configuration where  $h_2/h_1 = 1/5$  while  $\rho_2/\rho_1 = 0.859$ . The third case is related to the present physical experiments, where  $\rho_2/\rho_1 = 0.869$  and  $h_2/h_1 = 1/15$ . It is shown that the MCC-FS model can provide accurate results for the shallow configurations. Meanwhile, the HLGN-FS model is shown to be accurate for describing the internal solitary waves for both shallow and deep configurations.

**Key words:** internal solitary waves; High-Level Green-Naghdi model; two-layer fluid flow

## 1. Introduction

Internal solitary waves in the oceans are often caused by currents propagating over an uneven bottom or sea ridge. Internal solitary waves are observed in the oceans, such as the one with amplitude as large as 240m observed in the South China Sea by Huang *et al.* (2016). They can cause serious threats to submarines, offshore platforms, and marine risers, among others. Hence, it is of interest to investigate internal solitary waves, including the wave profile, velocity field and wave speed.

Large-amplitude internal solitary waves play an important role in nonlinear water

<sup>†</sup> Email address for correspondence: zhan.wang@hrbeu.edu.cn

waves. Both observations of Stanton & Ostrovsky (1998) (at northern Oregon Continental Shelf) and the theoretical models of Ostrovsky & Grue (2003) have shown that internal solitary waves with very large amplitudes (with respect to the upper layer depth) may be formed and remain stable. A similar wave was observed by Duda *et al.* (2004) in the South China Sea, where the wave amplitude was about four times the thickness of the mixed upper layer. Stable internal solitary waves with larger amplitudes are generated in laboratory environments, see e.g. Fructus *et al.* (2009). Large internal solitary waves may eventually become unstable and break due to either convective instability or shear-driven stresses, see e.g. Fructus *et al.* (2009), Lamb & Farmer (2011) and Carr *et al.* (2011). In this study, the breaking internal solitary waves are not considered.

Several laboratory experiments have been conducted on internal solitary waves in a two-layer fluid system. The common method for internal solitary wave generation at a laboratory is the gravity collapse method, used for example, by Kao *et al.* (1985), Michallet & Barthelémy (1997, 1998), Grue *et al.* (1999) and Kodaira *et al.* (2016). Among these experimental studies, Michallet & Barthelémy (1997, 1998) used ultrasonic probes to measure the wave profile at the interface. Grue *et al.* (1999) used particle tracking velocimetry (PTV) to measure the wave speed, wave profile and horizontal velocity distribution along the fluid column. Kodaira *et al.* (2016) used several wave probes to determine the profiles and speeds of internal solitary waves.

Numerical analysis of internal solitary waves is often carried out by use of the Korteweg-de Vries (KdV) equation. However, at such large amplitudes, internal solitary waves differ remarkably from the prediction of the KdV equation, see e.g. Miles (1980), Grue *et al.* (1999) and Kodaira *et al.* (2016). For more details on the KdV equation and its application to this problem, we refer the reader to Ostrovsky & Stepanyants (2005) and Helfrich & Melville (2006).

Strongly nonlinear models are required to study the generation and propagation of such nonlinear wave motions, see Grue (2006). Some efficient theoretical or numerical studies have been developed under the assumption that the free surface is a rigid lid, i.e. the rigid-lid (RL) assumption. For the two-layer fluid system, it is discussed by Camassa *et al.* (2006) that when the wavelength is long compared with the fluid layer depths (i.e.  $h_2/\lambda \ll 1$  and  $h_1/\lambda \ll 1$ , where  $h_2, h_1$  are the depths of the upper fluid layer and the lower fluid layer, respectively, and  $\lambda$  is the characteristic wavelength), it belongs to the ‘shallow configuration’. On the other hand, when the depth of one fluid layer is much larger than the other, while being comparable to or larger than the wavelength (e.g.  $h_2/\lambda \ll 1$  and  $h_1/\lambda = O(1)$ ), it belongs to the ‘deep configuration’. Miyata (1985, 1988) and Choi & Camassa (1999) derived a strongly nonlinear model for a shallow configuration. In their model, the velocity field was described by use of the depth-averaged horizontal velocities. This model is called the MCC (Miyata, Choi, Camassa) model. Here we refer to it as the MCC-RL model since the rigid-lid assumption was used. Because of its simple form and release of the assumption of small-amplitude motions, the MCC-RL model is widely used to study relatively large-amplitude internal solitary waves for a shallow configuration. Grue *et al.* (1999) obtained the internal solitary-wave solutions by solving Euler’s equations subject to the rigid-lid assumption, i.e. Euler-RL solution. The numerical results of Grue *et al.* (1999) showed very good agreement with the experimental data on the wave profile and velocity field for the case of  $h_2/h_1 = 1/4.13$  and  $\rho_2/\rho_1 = 0.977$ , where  $\rho_2, \rho_1$  are the densities of the upper-fluid layer and the lower-fluid layer, respectively.

Meanwhile, some other models under the rigid-lid assumption for a deep configuration have been employed. Choi & Camassa (1999) developed a strongly nonlinear model for a deep configuration. In this model, the depth-averaged velocity approximation was applied

to describe the upper-layer velocity field, and the linear theory was applied to describe the lower-layer velocity field. Results showed some differences between this model and Euler-RL solution for a deep-configuration case. Debsarma *et al.* (2010) improved the deep-water model of Choi & Camassa (1999) and Camassa *et al.* (2006), and increased the approximation to  $O(\epsilon^2)$  terms, where  $\epsilon = h_2/\lambda$ . Some differences between Euler-RL solution and the results given by Debsarma *et al.* (2010) for the deep-configuration case were observed. Recently, Zhao *et al.* (2016) developed the two-layer High-Level Green-Naghdi model under the rigid-lid assumption (HLGN-RL model). The HLGN-RL results showed very good agreement with Euler-RL solution on the wave profile, velocity field and wave speed for strongly nonlinear internal solitary waves for a deep configuration.

For relatively large density differences between the two fluids, e.g.  $\rho_2/\rho_1 = 0.859$  that was tested by Kodaira *et al.* (2016), the free-surface effects are not negligible and should be considered. The presence of the free surface introduces further challenges to the problem due to (i) the interaction between the surface and internal waves, and (ii) the difference in motion scale of the surface and internal waves. Choi & Camassa (1996) derived the MCC model that included the free-surface effects (MCC-FS model). Kodaira *et al.* (2016) showed that the wave profiles obtained by the MCC-FS model matched the experimental data very well, even for the large-amplitude internal solitary waves. Also, a comparative study between the MCC-RL results and the MCC-FS results on the wave profiles and wave speeds were presented by Kodaira *et al.* (2016). They showed that the wave profiles obtained by the MCC-RL model were wider and the wave speeds were larger than the results obtained by the MCC-FS model. Forgia & Sciotino (2019) conducted experiments on internal solitary waves with a free surface and measured the maximum surface elevation right above the trough of the internal solitary wave. They showed that the maximum surface elevation increased (with respect to the upper layer depth) with smaller density ratio  $\rho_2/\rho_1$ , and smaller depth ratio  $h_2/h_1$ .

To our knowledge, comparative studies between experiments and numerical results on internal solitary waves with a free surface for deep-configuration cases has not been performed before. The goals of this study are (i) to conduct laboratory experiments on strongly nonlinear internal solitary waves with a free surface for a deep configuration, (ii) to compare the results provided by the MCC-FS model with the present experimental data to test its capability, and (iii) to develop a strongly nonlinear internal solitary-wave model for a deep configuration and test its capability through some test cases.

In Section 2, the laboratory experiments and the MCC-FS results are presented. The two-layer High-Level Green-Naghdi equations that include the free-surface effects (HLGN-FS equations) are derived in Section 3. The algorithm to solve the HLGN-FS equations is shown in Section 4. The HLGN-FS results, MCC-FS results, experimental data from literature and present experimental data are presented and discussed in Section 5. Conclusions are reached in Section 6.

## 2. Laboratory experiments

Laboratory experiments are conducted to study the strongly nonlinear internal solitary waves with a free surface for a deep configuration, and when the density ratio between the two fluids is not necessarily close to 1. The laboratory experiments are conducted at the Harbin Engineering University (HEU) of China and details are provided below. Internal solitary waves propagate as a depression when the interface between the two fluids is closer to the free surface than the bed. In this study, attention is confined to internal solitary waves of depression form.

### 2.1. Experimental facility and set-up

The laboratory experiments are conducted in a wave tank designed and built specifically for this study. The tank is 400cm long, 15cm wide, with a total depth of 50cm. The tank walls are made of glass. In all laboratory tests, the lower-fluid layer is fresh water ( $\rho_1 = 997\text{kg/m}^3$ ) and the upper-fluid layer is silicone oil ( $\rho_2 = 866.5\text{kg/m}^3$ ). To add the two fluids in the tank, first fresh water is added as the lower fluid. A polystyrene foam sheet, with mass density smaller than the fresh water, is used to reduce the disturbance when adding the silicone oil to the tank. The polystyrene foam is distributed uniformly over the fresh water and the silicone oil is added gradually through the foam sheet. The sheet is removed before the start of the experiments. Overall, using this approach, little to no mixing is observed. Figure 1(a) shows the physical wave tank and Figure 1(b) shows the schematic of the wave tank. The top layer is open to the atmosphere.

To generate the internal solitary waves, the gravity collapse method (see Kao *et al.* (1985)) is used. Once the two fluid layers are filled and settled, a gate is placed at 25cm away from the left wall of the tank. A prescribed volume of silicone oil with depth  $d$  is added behind the gate, see Figure 1.

A pulley system is designed and used to remove the gate automatically and rapidly. One side of the pulley system is a weight that is connected by an electromagnetic relay, and the other side is the gate. Figure 2 shows the schematic of the pulley system. At the beginning of each test (corresponding to  $t = 0\text{s}$ ), the power supply of the electromagnet relay is cut off. The weight then goes into free fall and it removes the gate quickly, resulting in generation of a single solitary wave of depression form. The wave then propagates to the right in the main section of the tank. Figure 3 shows a snapshot of an internal solitary wave propagating in the tank.

### 2.2. Measurements

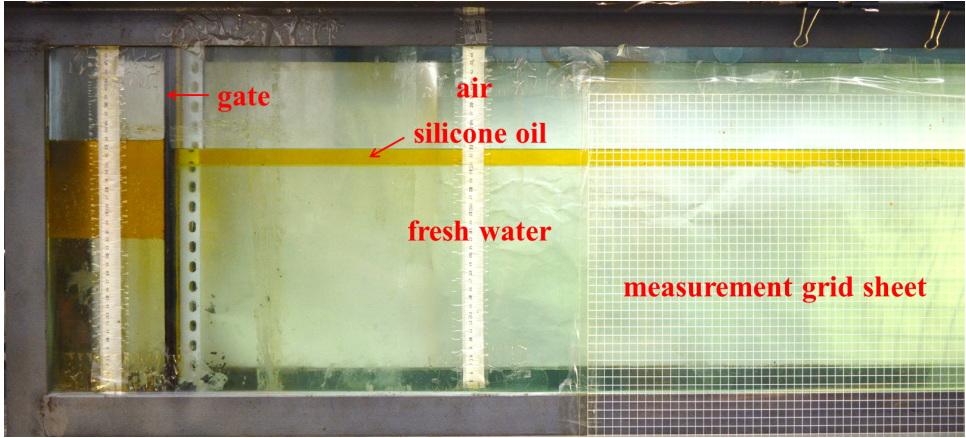
The internal solitary waves generated by the removal of the gate, propagate along the interface of the two fluids to the right. Measurements focus on the internal-wave profile. A digital camera capable of recording videos at 60 fps is used. A transparent reference grid sheet, 120cm long, 1cm  $\times$  1cm size per grid, is fixed to the tank wall at 55cm away from the gate. The location of the transparent grid sheet is chosen such that it is far from the right boundary to avoid any reflections during the measurements. The vertical location of the grid sheet is chosen carefully to cover the entire wave. The digital camera is located right in front of the transparent grid sheet and level with the interface of the fluids and recorded the motion of the internal solitary wave.

Recordings of the camera as the wave passed through the grid sheet are used to determine the wave profile. A sample recording of the internal solitary wave passing behind the sheet is shown in Figure 4, where the  $ox$  axis is set at the undisturbed interface and the internal solitary-wave amplitude  $a$  and profile  $z = \eta_1(x, t)$  are shown. The *GetData Graph Digitizer* software is used to obtain the front half profile of the internal solitary wave manually. Careful attention is given to read the profiles of all cases at about the same location across the grid sheet, when the wave is right in front of the lens. The measurement error is  $\varepsilon \approx \pm 0.06\text{cm}$  along the vertical direction due to the resolution of the recording picture and *GetData Graph Digitizer* software. Each test is conducted twice to assess the repeatability of the experiments.

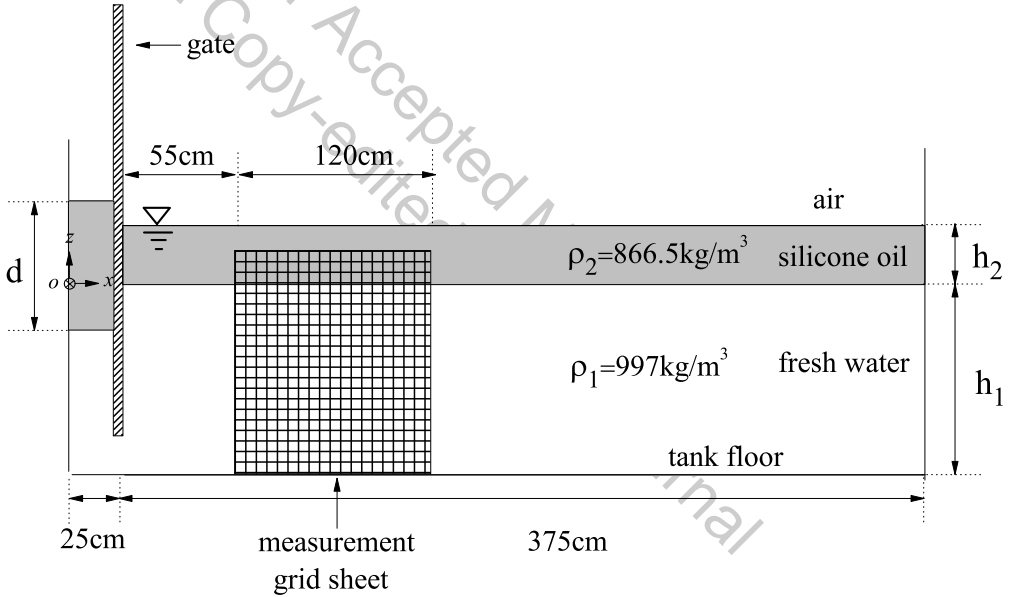
### 2.3. Experimental cases and the MCC-FS results

The upper and lower fluids (silicone oil and water, respectively) are kept the same in all laboratory experiments resulting in the relative density ratio of  $\rho_2/\rho_1 = 0.869$ .





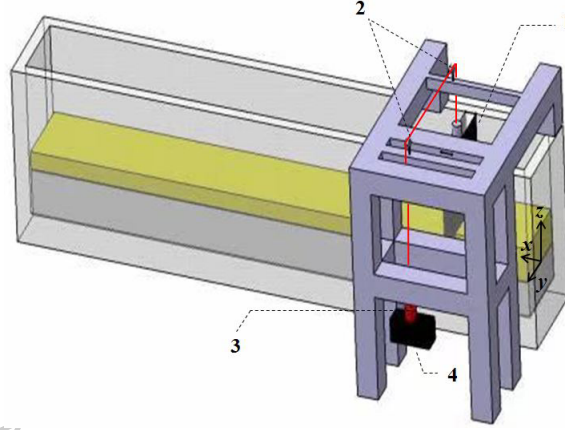
(a) The physical wave tank.



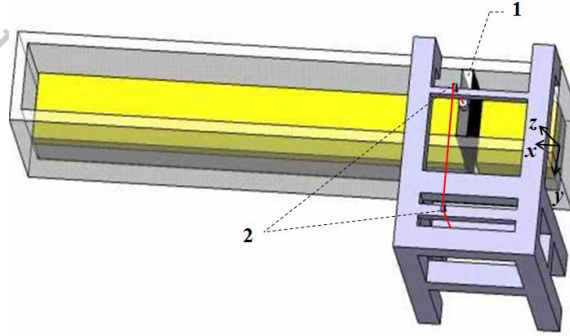
(b) Schematic of the wave tank. Figure not to scale.

Figure 1: Set-up of the experiments on internal solitary waves in a two-layer fluid system with a free surface.

In all laboratory experiments, the depths of the lower and upper layers are fixed at  $h_1 = 30\text{cm}$  and  $h_2 = 2\text{cm}$ , respectively, corresponding to the depth ratio of  $h_2/h_1 = 1/15$ . Three initial depths (volumes in three dimensions) of the silicone oil behind the gate are considered, namely  $d = 8\text{cm}$ ,  $d = 10\text{cm}$  and  $d = 12\text{cm}$ . As a result, we obtained the internal solitary waves with the amplitudes of  $a/h_2 = -1.41, -1.91$  and  $-2.35$ . The parameters of the physical experiments are given in Table 1.



(a) Side view.



(b) Plan view.

Figure 2: Sketch of the pulley system, showing: 1. gate, 2. pulley, 3. electromagnetic relay, and 4. weight.

---

Case	$h_2(\text{cm})$	$h_1(\text{cm})$	$d(\text{cm})$	$a(\text{cm})$	$h_2/h_1$	$a/h_2$
a	2	30	8	-2.83	1/15	-1.41
b	2	30	10	-3.83	1/15	-1.91
c	2	30	12	-4.71	1/15	-2.35

---

Table 1: Parameters and results of the physical experiments conducted at the internal wave flume of HEU.

It was found that for a given collapse height, solitary waves generated by complete removal of the gate have larger amplitudes than those generated by partial removal of the gate. In either methods of partial or complete removal of the gate, solitary waves with desired amplitudes can be generated by carefully adjusting the initial collapse height. We observed no differences between the profile of solitary waves of the same amplitude, whether generated by complete or partial removal of the gate. Internal solitary waves in this paper are generated by partial removal of the gate. Results of the two repeats of the laboratory measurements are shown in Figure 5. Also shown in the figure is the results





Figure 3: Snapshot of an internal solitary wave propagating in the tank approximately at  $t = 4s$  (the gate is removed completely at  $t = 0s$ ).

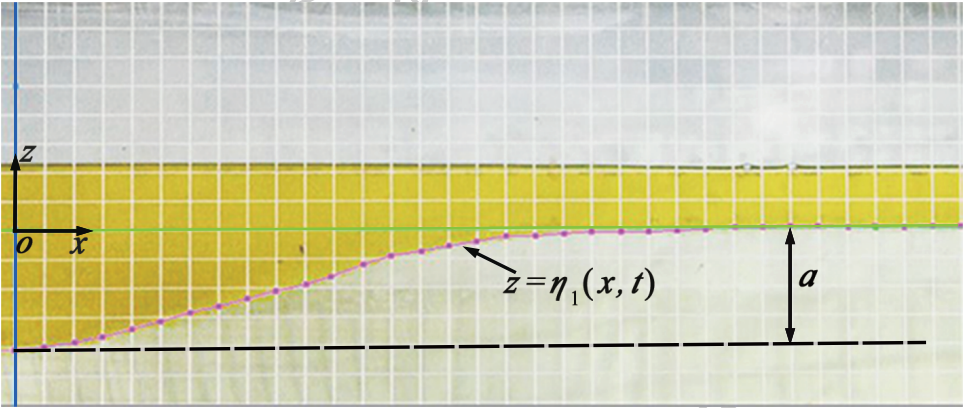
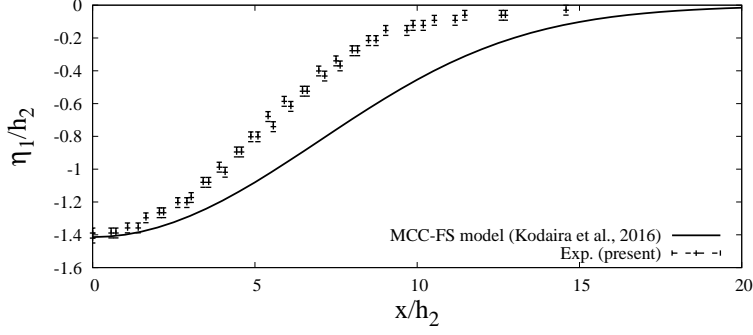
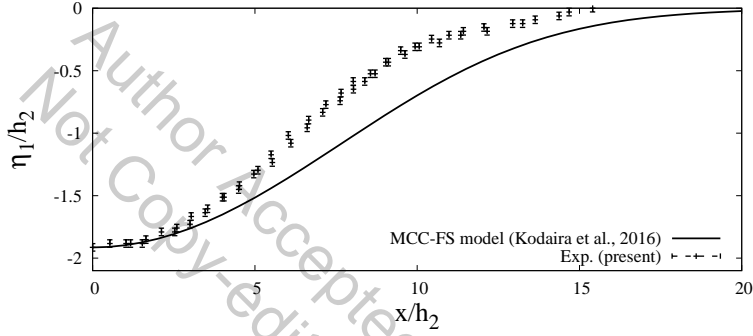
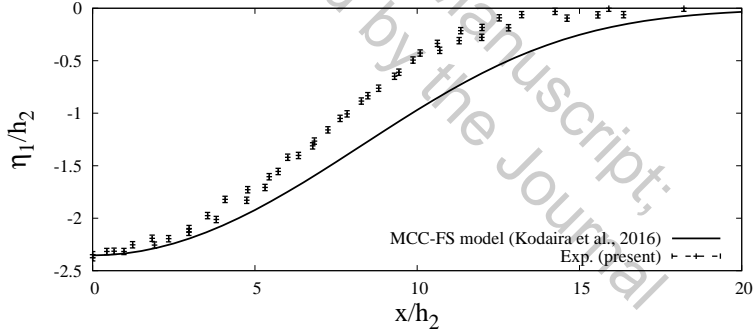


Figure 4: A sample recording of the internal solitary wave behind the transparent sheet.

of the MCC-FS model of Kodaira *et al.* (2016), included for comparisons. We find that the physical experiments are repeatable. From the comparison, it is clear that the wave profiles obtained by the MCC-FS model are much wider than the physical experimental measurements. This is not surprising given that the case of  $h_2/h_1 = 1/15$  belongs to the deep configuration, and the MCC model is valid only for a shallow configuration, see Camassa *et al.* (2006).

Hence, it is concluded that for the present case of the density ratio  $\rho_2/\rho_1 = 0.869$  and depth ratio  $h_2/h_1 = 1/15$ , the MCC-FS model does not accurately describe the internal solitary waves with a free surface. Instead, a strongly nonlinear model for a deep configuration is required to solve such a problem accurately.

(a)  $a/h_2 = -1.41$ .(b)  $a/h_2 = -1.91$ .(c)  $a/h_2 = -2.35$ .Figure 5: Profiles of internal solitary waves,  $\rho_2/\rho_1 = 0.869$ ,  $h_2/h_1 = 1/15$ .

### 3. Two-layer HLG-N-FS equations

In this section, we will develop the two-layer High-Level Green-Naghdi (HLGN) model that includes the free-surface effects (HLGN-FS model). Here the two-dimensional model is considered, although this is not a requirement in general. The fluid is assumed inviscid and incompressible. The coordinate origin is set at the still interface surface.  $x$  is the horizontal axis, positive to the right, and  $z$  is the vertical axis, positive up.

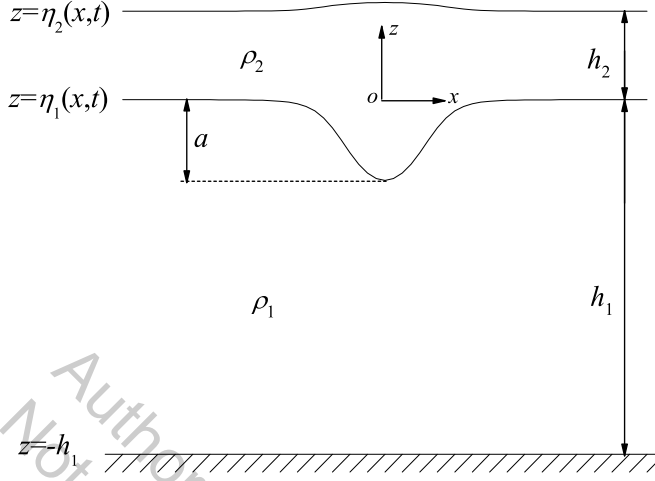


Figure 6: Setup of the theoretical tank of internal solitary wave generation and propagation in a two-layer fluid system with a free surface.

For both the upper layer and the lower layer, the continuity equation is written as

$$\frac{\partial u}{\partial x} + \frac{\partial w}{\partial z} = 0, \quad (3.1)$$

where  $u$  and  $w$  are the velocity components in the  $x$  and  $z$  directions, respectively.

The Euler equations are written as

$$\frac{\partial u}{\partial t} + u \frac{\partial u}{\partial x} + w \frac{\partial u}{\partial z} = -\frac{1}{\rho} \frac{\partial p}{\partial x}, \quad (3.2a)$$

$$\frac{\partial w}{\partial t} + u \frac{\partial w}{\partial x} + w \frac{\partial w}{\partial z} = -\frac{1}{\rho} \left( \frac{\partial p}{\partial z} + \rho g \right), \quad (3.2b)$$

where  $t$  is the time,  $\rho$  is the mass density of the fluid,  $p$  is the pressure and  $g$  is the gravitational acceleration.

In this paper, the free surface, interface and bottom boundary are expressed by  $z = \eta_2(x, t)$ ,  $z = \eta_1(x, t)$  and  $z = -h_1$  respectively, where  $h_1$  is constant.  $\rho_2$  is the mass density of the upper layer fluid and  $\rho_1$  is the mass density of the lower layer fluid, also shown in Figure 6.

The kinematic boundary conditions are expressed as

$$w^U = \frac{\partial \eta_2}{\partial t} + u^U \frac{\partial \eta_2}{\partial x} \quad z = \eta_2(x, t), \quad (3.3a)$$

$$w^U = \frac{\partial \eta_1}{\partial t} + u^U \frac{\partial \eta_1}{\partial x} \quad z = \eta_1(x, t), \quad (3.3b)$$

$$w^L = \frac{\partial \eta_1}{\partial t} + u^L \frac{\partial \eta_1}{\partial x} \quad z = \eta_1(x, t), \quad (3.3c)$$

$$w^L = 0 \quad z = -h_1, \quad (3.3d)$$

where the superscripts ‘ $U$ ’ and ‘ $L$ ’ indicate the variable in the upper layer and lower layer, respectively.

In the HLGN model, e.g. Zhao *et al.* (2016), the velocity field is given as

$$u^U(x, z, t) = \sum_{n=0}^{K^U} u_n^U(x, t) z^n, \quad w^U(x, z, t) = \sum_{n=0}^{K^U} w_n^U(x, t) z^n, \quad (3.4a)$$

$$u^L(x, z, t) = \sum_{n=0}^{K^L} u_n^L(x, t) z^n, \quad w^L(x, z, t) = \sum_{n=0}^{K^L} w_n^L(x, t) z^n, \quad (3.4b)$$

where  $K^U$  is the level of the HLGN model applied for the upper layer and  $K^L$  is the level of the HLGN model applied for the lower layer, respectively.  $K^U$  and  $K^L$  can be chosen independent of each other. We use HLGN- $K^U$ - $K^L$  to indicate which level we use for each layer (in this paper, we select  $K^U = K^L$  to obtain the converged HLGN results but this is not necessary in general).  $u_n^U, w_n^U, u_n^L, w_n^L$  are the unknown velocity coefficients that are determined as part of the solution.

Substituting Eqs. (3.4) into Eq. (3.1) results in the following relations:

$$u_{K^U}^U = 0, \quad (3.5a)$$

$$w_n^U = -\frac{1}{n} \frac{\partial u_{n-1}^U}{\partial x} \quad n = 1, 2, \dots, K^U, \quad (3.5b)$$

$$u_{K^L}^L = 0, \quad (3.5c)$$

$$w_n^L = -\frac{1}{n} \frac{\partial u_{n-1}^L}{\partial x} \quad n = 1, 2, \dots, K^L. \quad (3.5d)$$

Substituting Eqs. (3.4) into Eq. (3.2), and multiplying each term by  $z^n$  and integrating from  $\eta_1$  to  $\eta_2$  for the upper layer, and from  $-h_1$  to  $\eta_1$  for the lower layer, will result in

$$\begin{aligned} & \frac{\partial}{\partial x} (G_n^U + gS1_n^U) + nE_{n-1}^U - \eta_1^n \frac{\partial}{\partial x} (G_0^U + gS1_0^U) \\ & + (\eta_2^n - \eta_1^n) \frac{\partial}{\partial x} \left( \frac{\hat{p}^U}{\rho_2} \right) = 0 \quad n = 1, 2, \dots, K^U, \end{aligned} \quad (3.6a)$$

$$\begin{aligned} & \frac{\partial}{\partial x} (G_n^L + gS1_n^L) + nE_{n-1}^L - (-h_1)^n \frac{\partial}{\partial x} (G_0^L + gS1_0^L) \\ & + (\eta_1^n - (-h_1)^n) \frac{\partial}{\partial x} \left( \frac{\hat{p}^L}{\rho_1} \right) = 0 \quad n = 1, 2, \dots, K^L, \end{aligned} \quad (3.6b)$$

where  $\hat{p}^U = 0$  is the pressure at the upper surface of the upper layer (without loss in generality),  $\hat{p}^L$  is the pressure at the upper surface of the lower layer that equals the pressure at the lower surface of the upper layer  $\bar{p}^U$ , which is written as

$$\hat{p}^L = \bar{p}^U = \rho_2 G_0^U + \rho_2 g S1_0^U, \quad (3.7)$$

and

$$E_n^U = \sum_{m=0}^{K^U} \left( \frac{\partial u_m^U}{\partial t} S2_{mn}^U + \frac{\partial u_m^U}{\partial x} Q_{mn}^U + u_m^U H_{mn}^U \right), \quad (3.8a)$$

$$G_n^U = \sum_{m=0}^{K^U} \left( \frac{\partial w_m^U}{\partial t} S2_{mn}^U + \frac{\partial w_m^U}{\partial x} Q_{mn}^U + w_m^U H_{mn}^U \right), \quad (3.8b)$$

$$Q_{mn}^U = \sum_{r=0}^{K^U} u_r^U S3_{mrn}^U, \quad H_{mn}^U = \sum_{r=0}^{K^U} w_r^U S4_{mrn}^U, \quad (3.8c)$$

$$S1_n^U = \int_{\eta_1}^{\eta_2} z^n dz, \quad S2_{mn}^U = \int_{\eta_1}^{\eta_2} z^{m+n} dz, \quad (3.8d)$$

$$S3_{mrn}^U = \int_{\eta_1}^{\eta_2} z^{m+r+n} dz, \quad S4_{mrn}^U = m \int_{\eta_1}^{\eta_2} z^{m+r+n-1} dz. \quad (3.8e)$$

We note that the expression for the lower layer is obtained by changing ‘ $U$ ’ to ‘ $L$ ’,  $\eta_1$  to  $-h_1$  and  $\eta_2$  to  $\eta_1$  in Eq. (3.8).

Substituting Eq. (3.4) into Eq. (3.3), we obtain

$$\frac{\partial \eta_2}{\partial t} = \sum_{n=0}^{K^U} \eta_2^n \left( w_n^U - \frac{\partial \eta_2}{\partial x} u_n^U \right), \quad (3.9a)$$

$$w_0^U = \frac{\partial \eta_1}{\partial t} + \frac{\partial \eta_1}{\partial x} u_0^U + \sum_{n=1}^{K^U} \eta_1^n \left( \frac{1}{n} \frac{\partial u_{n-1}^U}{\partial x} + \frac{\partial \eta_1}{\partial x} u_n^U \right), \quad (3.9b)$$

$$\frac{\partial \eta_1}{\partial t} = \sum_{n=0}^{K^L} \eta_1^n \left( w_n^L - \frac{\partial \eta_1}{\partial x} u_n^L \right), \quad (3.9c)$$

$$w_0^L = \sum_{n=1}^{K^L} \frac{(-h_1)^n}{n} \frac{\partial u_{n-1}^L}{\partial x}. \quad (3.9d)$$

There is no gap at the interface between the two fluids at any time by assumption. Hence, solutions of the two layers are coupled at the interface. Therefore, we can eliminate  $w_n^U$  and  $w_n^L$  by using Eqs. (3.5b), (3.5d), (3.9b) and (3.9d). As a result, the unknowns are  $\eta_2$ ,  $\eta_1$ ,  $u_n^U$  ( $n = 0, 1, \dots, K^U - 1$ ) and  $u_n^L$  ( $n = 0, 1, \dots, K^L - 1$ ). The number of unknowns is  $K^U + K^L + 2$ . On the other hand, the number of equations, including Eqs. (3.6), (3.9a) and (3.9c), is also  $K^U + K^L + 2$ . Hence, the problem is closed.

#### 4. Solution algorithm

In the HLG-N-FS equations, Eq. (3.6) is expressed by

$$\mathbf{A} \dot{\xi}_{,xx} + \mathbf{B} \dot{\xi}_{,x} + \mathbf{C} \dot{\xi} = \mathbf{f}, \quad (4.1)$$

where  $\mathbf{A}$ ,  $\mathbf{B}$  and  $\mathbf{C}$  are  $(K^U + K^L) \times (K^U + K^L)$  matrices,  $\mathbf{f}$  is a  $(K^U + K^L)$  vector and

$$\dot{\xi}(x, t) = [\dot{u}_0^U, \dot{u}_1^U, \dots, \dot{u}_{K^U-1}^U, \dot{u}_0^L, \dot{u}_1^L, \dots, \dot{u}_{K^L-1}^L]^T. \quad (4.2)$$

The dot over a variable indicates time derivative, i.e.  $\dot{\xi} = \partial \xi / \partial t$ , and the subscript after comma is differentiation with respect to the indicated variable.  $\mathbf{A}$ ,  $\mathbf{B}$ ,  $\mathbf{C}$  and  $\mathbf{f}$  are functions of  $\eta_1(x, t)$ ,  $\eta_2(x, t)$ ,  $\xi(x, t)$  and their spatial derivatives. For simplification, this dependence will not be shown here.

The above system of differential equations are solved by use of the spatial finite-difference discretization. The domain of  $x$  over which a solution to the equations is desired is assumed to have a uniform grid of  $x$  values, spaced a distance of  $\Delta x$  apart. The  $i^{th}$  point on the grid is denoted by  $x_i = i\Delta x$  for  $i = 1, 2, \dots, nx$ . Time is discretized with intervals  $\Delta t$ , with  $t_j = j\Delta t$ . The value of the solution vector  $\xi(x_i, t_j)$  will be denoted by  $\xi^{(i)}$  ( $j$  is omitted in the following part, because we refer to the same  $j$  time) and similar superscripts will be used for other vectors and matrices. The spatial derivatives  $\dot{\xi}_{,x}$  and  $\dot{\xi}_{,xx}$  are approximated by the five-point central difference scheme as

$$\dot{\xi}_{,x}^{(i)} = \frac{1}{12\Delta x}(\dot{\xi}^{(i-2)} - 8\dot{\xi}^{(i-1)} + 8\dot{\xi}^{(i+1)} - \dot{\xi}^{(i+2)}), \quad (4.3a)$$

$$\dot{\xi}_{,xx}^{(i)} = \frac{1}{12\Delta x^2}(-\dot{\xi}^{(i-2)} + 16\dot{\xi}^{(i-1)} - 30\dot{\xi}^{(i)} + 16\dot{\xi}^{(i+1)} - \dot{\xi}^{(i+2)}). \quad (4.3b)$$

The five-point central difference scheme provides fourth-order accuracy for the first and second derivatives, and second-order accuracy for the third derivative. With these approximations, Eq. (4.1) can now be written as

$$\tilde{\mathbf{A}}^{(i)}\dot{\zeta}^{(i-2)} + \tilde{\mathbf{B}}^{(i)}\dot{\zeta}^{(i-1)} + \tilde{\mathbf{C}}^{(i)}\dot{\zeta}^{(i)} + \tilde{\mathbf{D}}^{(i)}\dot{\zeta}^{(i+1)} + \tilde{\mathbf{E}}^{(i)}\dot{\zeta}^{(i+2)} = \mathbf{f}^{(i)}, \quad (4.4)$$

where

$$\tilde{\mathbf{A}}^{(i)} = -\mathbf{A}^{(i)}\frac{1}{12\Delta x^2} + \mathbf{B}^{(i)}\frac{1}{12\Delta x}, \quad (4.5a)$$

$$\tilde{\mathbf{B}}^{(i)} = \mathbf{A}^{(i)}\frac{16}{12\Delta x^2} - \mathbf{B}^{(i)}\frac{8}{12\Delta x}, \quad (4.5b)$$

$$\tilde{\mathbf{C}}^{(i)} = -\mathbf{A}^{(i)}\frac{30}{12\Delta x^2} + \mathbf{C}^{(i)}, \quad (4.5c)$$

$$\tilde{\mathbf{D}}^{(i)} = \mathbf{A}^{(i)}\frac{16}{12\Delta x^2} + \mathbf{B}^{(i)}\frac{8}{12\Delta x}, \quad (4.5d)$$

$$\tilde{\mathbf{E}}^{(i)} = -\mathbf{A}^{(i)}\frac{1}{12\Delta x^2} - \mathbf{B}^{(i)}\frac{1}{12\Delta x}. \quad (4.5e)$$

The algorithm to solve Eq. (4.4) can be found in Zhao *et al.* (2014). The algorithm obtains the values of  $\dot{u}_0^U, \dot{u}_1^U, \dots, \dot{u}_{K^U-1}^U, \dot{u}_0^L, \dot{u}_1^L, \dots, \dot{u}_{K^L-1}^L$ . In addition,  $\eta_1(x, t)$  and  $\eta_2(x, t)$  can be calculated by means of Eqs. (3.9a) and (3.9c). We then use the fourth-order Adams predictor-corrector scheme for time marching.

The initial values are given by the steady solution of the internal solitary waves with a free surface provided by the HLGN-FS model. For a similar method to obtain the steady solution, see Zhao *et al.* (2016) for details.

As an example, we show an internal solitary wave propagating at different times in Figure 7. The parameters are:  $\rho_2/\rho_1 = 0.859$ ,  $h_2/h_1 = 1/5$  and  $a/h_2 = -1.21$ . From  $t = 0$  to  $t = 60s$ , we find that the internal solitary wave propagates steadily. Meanwhile, since we use the pressure continuity condition at the interface given in Eq. (3.7) (rather than velocity continuity), velocity jump across the interface is allowed. This, however, does not have any affect on the numerical simulation. Numerical instability was observed for the MCC-RL model, shown by Jo & Choi (2008).

For comparison, in Figure 8 we plot the internal solitary wave (Figure 8(b)) and the free surface elevation (Figure 8(a)) of different times on top of each other. We observe that at  $t = 0s, 20s, 40s$  and  $60s$ , the wave profiles show very good agreement. Thus, we have obtained an accurate solution of the internal solitary waves with a free surface.



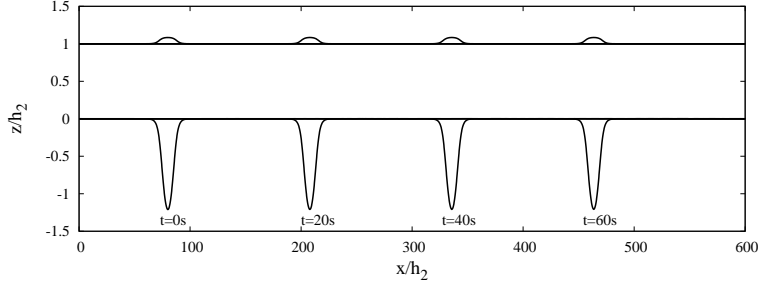
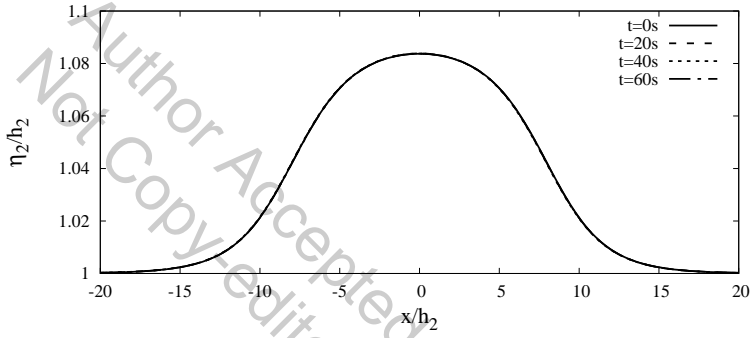
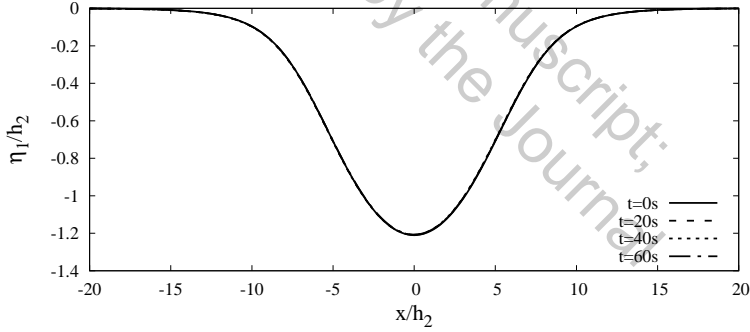


Figure 7: Snapshots of the theoretical internal solitary wave with a free surface at different times,  $\rho_2/\rho_1 = 0.859$ ,  $h_2/h_1 = 1/5$ ,  $a/h_2 = -1.21$ .



(a) Profiles of the waves on the free surface (lines are on top of each other).



(b) Profiles of internal solitary waves (lines are on top of each other).

Figure 8: Profiles of the internal solitary wave with a free surface at different times,  $\rho_2/\rho_1 = 0.859$ ,  $h_2/h_1 = 1/5$ ,  $a/h_2 = -1.21$ .

## 5. Results and discussion

In this section, three numerical cases are considered as shown in Table 2 and the solutions of internal solitary waves obtained by the HLG-N-FS model are presented, including the wave profile, velocity field and wave speed. We note that for each case, we have performed the HLG-N-FS self-convergence tests by using different  $K^U$  and  $K^L$  given in Eq. (3.4). We refer the reader to Zhao *et al.* (2014) and Zhao *et al.* (2016)

---

Case	Experiments by	$\rho_2/\rho_1$	$h_2/h_1$	$a/h_2$
1	Grue <i>et al.</i> (1999)	0.977	1/4.13	-0.36, -0.91, -1.23
2	Kodaira <i>et al.</i> (2016)	0.859	1/5	-0.50, -0.77, -1.21
3	present	0.869	1/15	-1.41, -1.91, -2.35

---

Table 2: Parameters of the numerical cases, and the laboratory experiments used for comparisons.

---

for the HLG-N convergence tests for details. The results presented in this paper are the converged HLG-N-FS results, which can be regarded as Euler's solution that includes the free-surface effects (Euler-FS solution).

### 5.1. $\rho_2/\rho_1 = 0.977, h_2/h_1 = 1/4.13$

Grue *et al.* (1999) conducted experiments on internal waves in a two-layer fluid system with a free surface. The rigid lid was set up on the free surface in their numerical simulations. Following the experiments of Grue *et al.* (1999), we select the parameters as  $h_1 = 0.62m$ ,  $h_2 = 0.15m$ ,  $\rho_1 = 1022kg/m^3$  and  $\rho_2 = 999kg/m^3$ .

Three different amplitudes are considered here; they are  $a/h_2 = -0.36, -0.91$  and  $-1.23$ . We compare the converged results of the HLG-N-FS model (HLG-N-3-3-FS results for this case) with the results of the HLG-N-RL model of Zhao *et al.* (2016) and the experimental data of Grue *et al.* (1999) as shown in Figure 9.

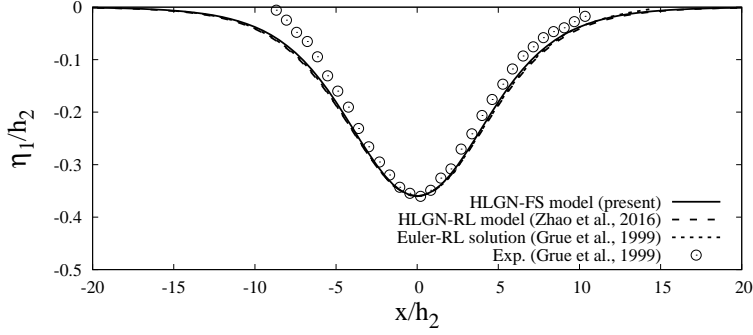
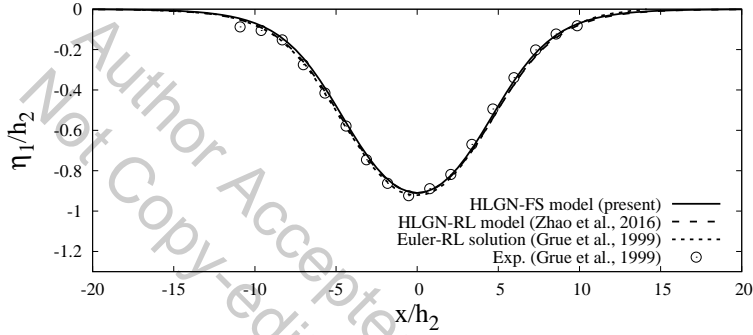
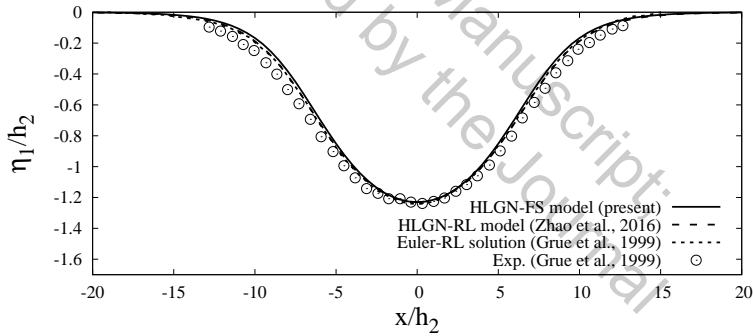
From Figure 9, we observe that the HLG-N-FS results and the HLG-N-RL results show very good agreement, both match Euler-RL solution and experimental data well, even for the strongly nonlinear cases.

We next show the wave profiles on the free surface obtained by the HLG-N-FS model and the MCC-FS model in Figure 10. From Figure 10, we find that a surface elevation exists at the free surface in each case. For the cases of internal solitary waves of  $a/h_2 = -0.36, -0.91$  and  $-1.23$ , the amplitudes of the surface waves,  $b$ , are  $b/h_2 = 0.5\%, 1.0\%$  and  $1.1\%$ , respectively. Thus, it is demonstrated here that the disturbance on the free surface is quite small for the cases of Grue *et al.* (1999). Meanwhile, we observe that the amplitudes of the surface wave predicted by the MCC-FS model show good agreement with the HLG-N-FS model, while the wave profiles are slightly wider for the MCC-FS model than these of the HLG-N-FS model.

Next, we focus on the horizontal velocity along the fluid column at the maximal displacement. The results of the HLG-N-FS model and the results of the HLG-N-RL model are shown in Figure 11, where the reference speed  $c_0 = \sqrt{\frac{gh_1h_2(\rho_1-\rho_2)}{\rho_2h_1-\rho_1h_2}}$  is the linear long wave speed. We find that the horizontal velocity predicted by the HLG-N-FS model shows good agreement with that predicted by the HLG-N-RL model. They both match Euler-RL solution of Grue *et al.* (1999) and experimental data very well as shown in Figure 11.

The relationship between the internal solitary wave amplitude  $|a|/h_2$  and exceedance wave speed  $c/c_0 - 1$  obtained by the HLG-N-FS model and HLG-N-RL model is shown in Figure 12. Figure 12 shows that the results of the HLG-N-FS model are close to the HLG-N-RL results and Euler-RL solution of Grue *et al.* (1999).

In general, in the cases with  $\rho_2/\rho_1 = 0.977$  and  $h_2/h_1 = 1/4.13$ , the results predicted by the HLG-N-FS model and the HLG-N-RL model agree very well with each other. This is because the mass densities between the upper-fluid layer and lower-fluid layer are very

(a)  $a/h_2 = -0.36$ .(b)  $a/h_2 = -0.91$ .(c)  $a/h_2 = -1.23$ .Figure 9: Profiles of internal solitary waves,  $\rho_2/\rho_1 = 0.977$ ,  $h_2/h_1 = 1/4.13$ .

close to each other, and hence the free surface disturbance is very small. Thus, it can be regarded as a rigid lid. This conclusion has been discussed previously, see e.g. Lamb (1932) and Kodaira *et al.* (2016).

## 5.2. $\rho_2/\rho_1 = 0.859$ , $h_2/h_1 = 1/5$

Kodaira *et al.* (2016) conducted experiments on internal waves in a two-layer fluid system. The mass densities of the lower-fluid layer and the upper-fluid layer are  $\rho_1 = 996 \text{ kg/m}^3$  and  $\rho_2 = 856 \text{ kg/m}^3$ , respectively. The depths are  $h_1 = 0.25 \text{ m}$  and  $h_2 = 0.05 \text{ m}$ , respectively. The gravity collapse method was used to generate internal solitary waves in

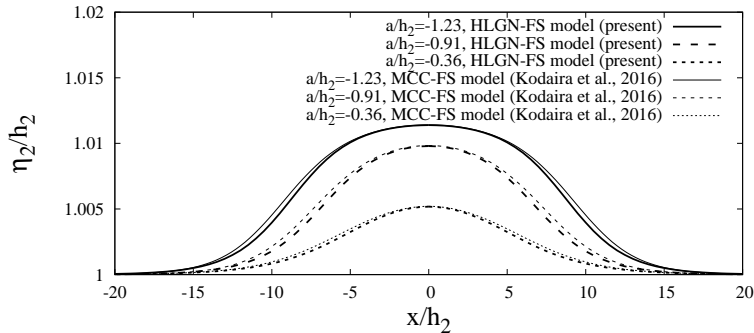


Figure 10: Profiles of waves on the free surface,  $\rho_2/\rho_1 = 0.977$ ,  $h_2/h_1 = 1/4.13$ .

the experiments. By adjusting the interface displacement behind the gate, five internal solitary waves with different amplitudes were generated; they are:  $a/h_2 = -0.24, -0.50, -0.77, -0.99$  and  $-1.21$ . In the numerical study of Kodaira *et al.* (2016), the MCC-RL model and the MCC-FS model were used to obtain the wave profiles and wave speed.

For simplification, we will show the results for three cases, namely the internal solitary waves with  $a/h_2 = -0.50, -0.77$  and  $-1.21$ . The wave profiles obtained by the HLG-N-RL model and the HLG-N-FS model are shown in Figs. 13-15, where the MCC-RL results and the MCC-FS results are also shown for comparison. The results provided by the models that are based on the rigid-lid assumption are not as accurate since the wave profiles they predict are wider than the experimental data, see Figures 13(a), 14(a) and 15(a). When we consider the free-surface effects, we find that both the converged HLG-N-FS results (HLG-N-3-3 results for this case) and the MCC-FS results show very good agreement with the experimental data, see Figures 13(b), 14(b) and 15(b). Thus, the effect of free surface is important in these cases.

Comparisons between the numerical results and the experimental data are not so good for the largest wave amplitude,  $a/h_2 = -1.21$  shown in Figure 15 for  $x/h_2 > 0$  part. This is similar to the case of internal solitary wave of  $a/h_2 = -1.51$  in the experiments conducted by Grue *et al.* (1999). Kodaira *et al.* (2016) pointed out that this large internal solitary wave suffered from the Kelvin-Helmholtz instability excited by the large shear across the interface.

The wave profiles on the free surface obtained by the MCC-FS model and the HLG-N-FS model for the cases of Kodaira *et al.* (2016) are shown in Figure 16. It is determined that for the cases of the internal solitary waves for  $a/h_2 = -0.50, -0.77$  and  $-1.21$ , the wave amplitudes on the free surface are  $b/h_2 = 4.8\%, 6.4\%$  and  $8.4\%$ . Thus, there are obvious disturbances on the free surface, and therefore it could not be regarded as a rigid lid. Again, we find that the MCC-FS model and the HLG-N-FS model predict the same amplitude of the surface wave. The profiles obtained by the MCC-FS model are wider than these obtained by the HLG-N-FS model.

The velocity distribution along the fluid column at the maximal displacement for the three cases determined by the HLG-N-FS model are shown in Figure 17. We also apply the modified velocity expression given by Camassa *et al.* (2006) for the MCC-FS model and obtain the velocity distribution shown in Figure 17 for comparison purposes. The MCC-FS results and the HLG-N-FS results match very well.

The relationship between the amplitude  $|a|/h_2$  and the exceedance wave speed  $c/c_0 - 1$

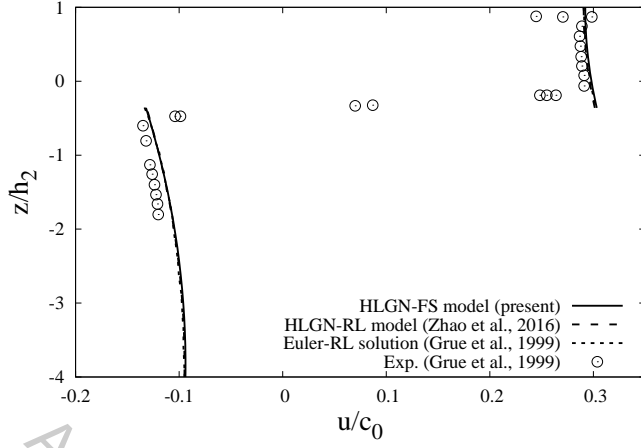
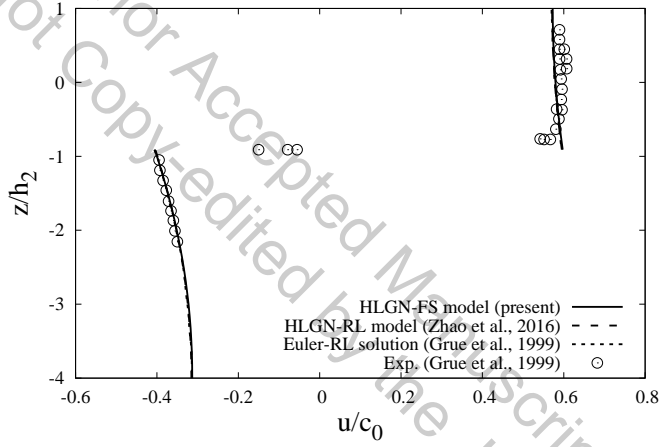
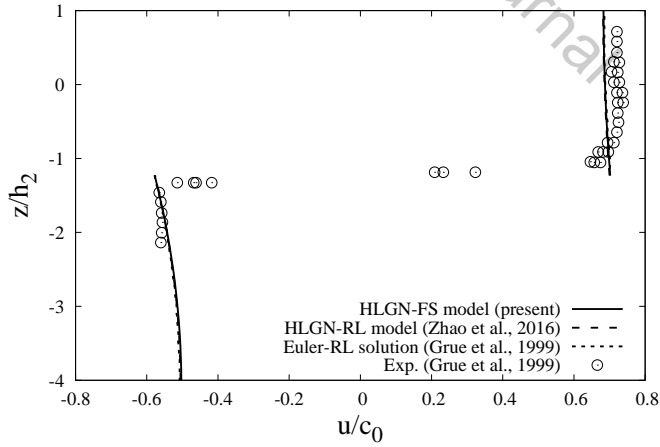
(a)  $a/h_2 = -0.36$ .(b)  $a/h_2 = -0.91$ .(c)  $a/h_2 = -1.23$ .

Figure 11: Horizontal velocity along the fluid column at maximal displacement,  $\rho_2/\rho_1 = 0.977$ ,  $h_2/h_1 = 1/4.13$ .

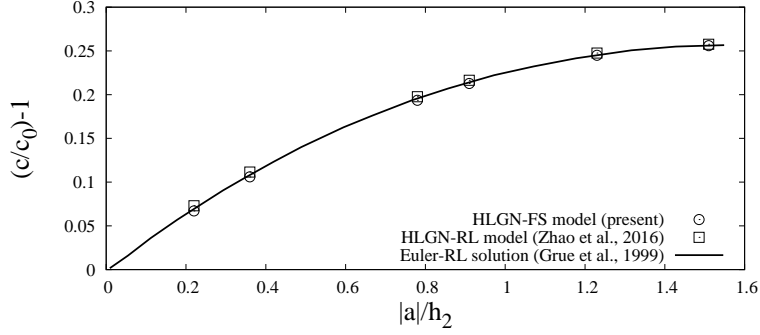
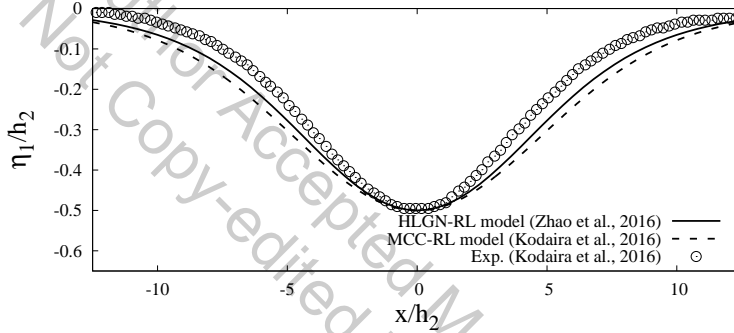
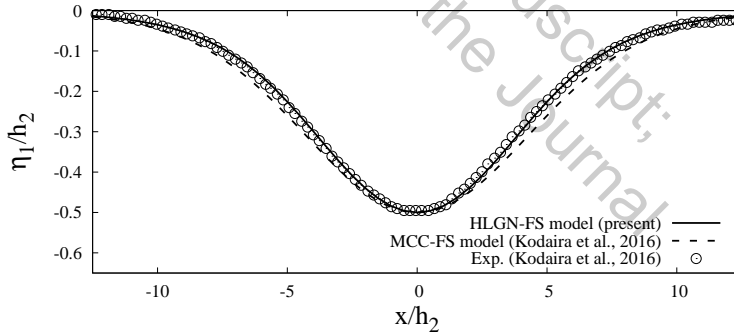


Figure 12: Excess propagation speed  $(c/c_0) - 1$  versus amplitude,  $\rho_2/\rho_1 = 0.977$ ,  $h_2/h_1 = 1/4.13$ .



(a) Rigid-lid assumption.



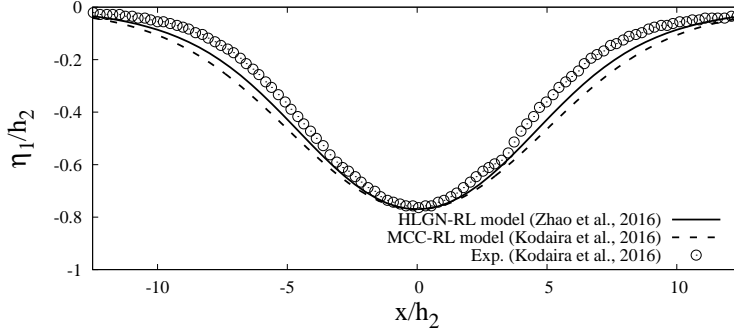
(b) With a free surface.

Figure 13: Profiles of internal solitary waves with  $a/h_2 = -0.50$ ,  $\rho_2/\rho_1 = 0.859$ ,  $h_2/h_1 = 1/5$ .

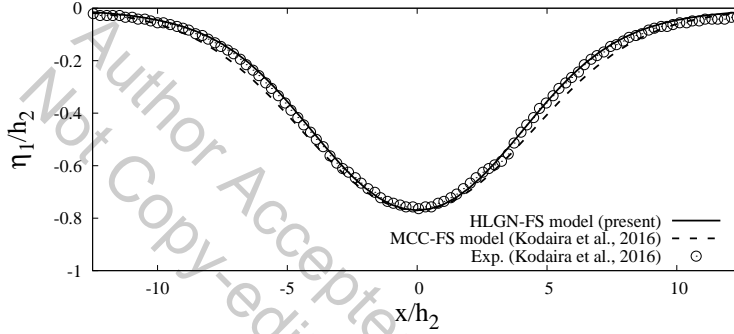
obtained by the HLGN-FS model and the MCC-FS model is shown in Figure 18. From Figure 18, it is found that the two models are in good agreement in general.

In this case, we find that when the density ratio between the two fluids is not close to 1 (e.g.  $\rho_2/\rho_1 = 0.859$ ), the rigid-lid assumption does not provide accurate description of the internal solitary waves. Instead, the models that include the free-surface effects





(a) Rigid-lid assumption.



(b) With a free surface.

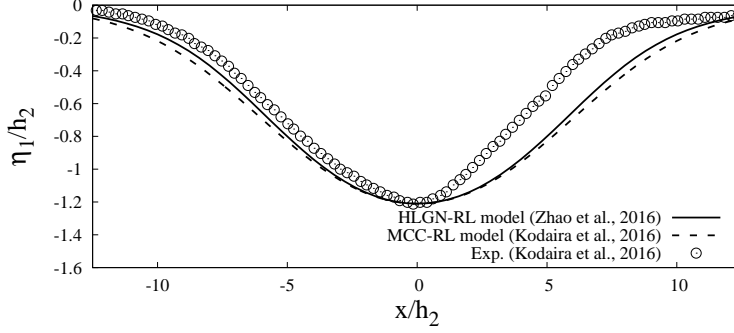
Figure 14: Profiles of internal solitary waves with  $a/h_2 = -0.77$ ,  $\rho_2/\rho_1 = 0.859$ ,  $h_2/h_1 = 1/5$ .

should be applied. The MCC-FS model and the HLG-N-FS model both describe the strongly nonlinear internal solitary waves with a free surface for the shallow configuration accurately.

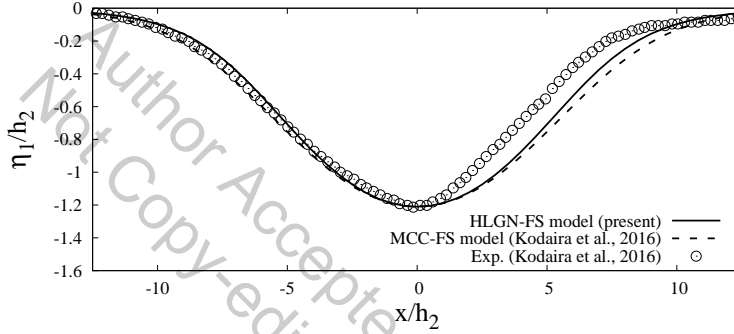
### 5.3. $\rho_2/\rho_1 = 0.869$ , $h_2/h_1 = 1/15$

Next, we study a case where the depth ratio  $h_2/h_1$  is significantly smaller than other cases. Here, we consider the case of  $\rho_2/\rho_1 = 0.869$  and  $h_2/h_1 = 1/15$ . This is the same case as used in our laboratory experiments, see Table 1 for the parameters. Here, we use the HLG-N-FS model to calculate the strongly nonlinear internal solitary waves for deep configuration. The internal solitary wave profiles of this case are shown in Figure 19. We also use the MCC-FS model in this case for comparison purposes. After having the self-convergence test of the HLG-N-FS model, it is determined that the HLG-N-5-5-FS model can provide converged HLG-N-FS results. We find that the converged HLG-N-FS results match the experimental data very well. However, the MCC-FS results show large errors compared with the experimental data.

We then use the MCC-FS model and the HLG-N-FS model to obtain the wave profiles on the free surface. Results are shown in Figure 20. We find that for the cases of  $a/h_2 = -1.41$ ,  $-1.91$  and  $-2.35$ , the wave amplitudes on the free surface are  $b/h_2 = 11.6\%$ ,  $14.4\%$  and  $16.6\%$  obtained by the HLG-N-FS model. Meanwhile, for this deep-configuration case, we find that the surface-wave profiles obtained by the MCC-FS model are obviously



(a) Rigid-lid assumption.



(b) With a free surface.

Figure 15: Profiles of internal solitary waves with  $a/h_2 = -1.21$ ,  $\rho_2/\rho_1 = 0.859$ ,  $h_2/h_1 = 1/5$ .

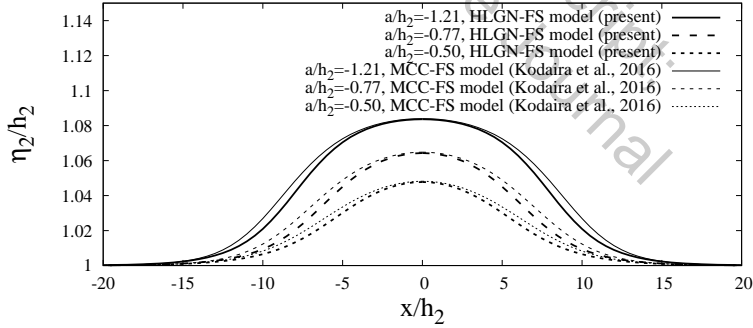


Figure 16: Wave profiles on the free surface.

higher and wider than these obtained by the HLGN-FS model. Meanwhile, similar to Forgia & Sciotino (2019), we measured the maximum surface elevation of the top fluid layer recorded in the laboratory experiments as shown in Figure 20. Good agreement is found between the numerical results and the experimental data.

We note that in the experiments of Kodaira *et al.* (2016), surface disturbance is observed towards the front of the internal solitary wave, and not over the trough. This

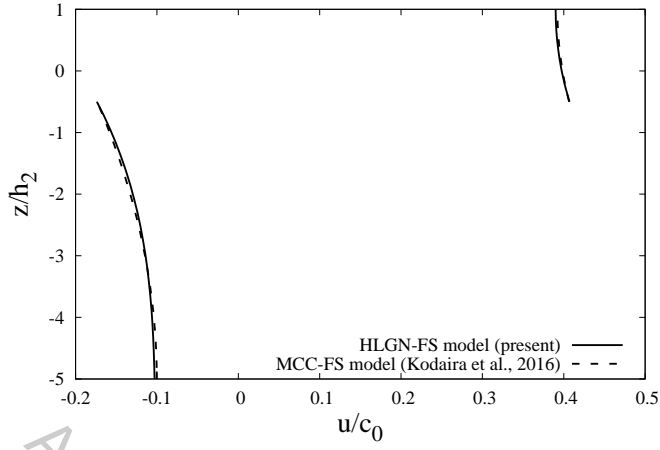
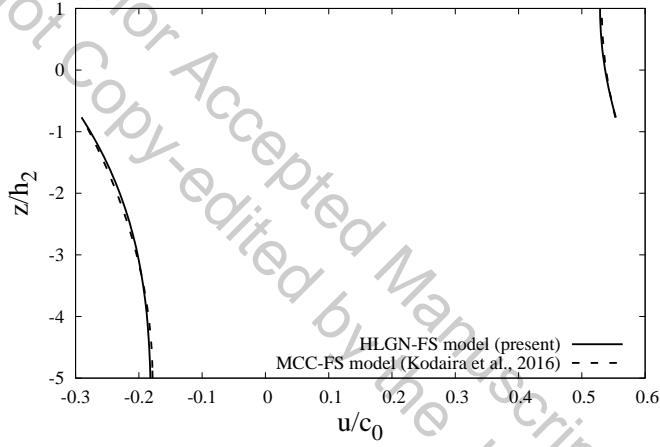
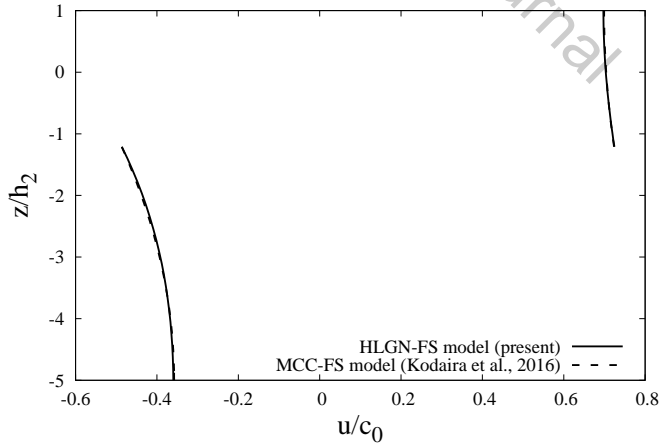
(a)  $a/h_2 = -0.50$ .(b)  $a/h_2 = -0.77$ .(c)  $a/h_2 = -1.21$ .

Figure 17: Horizontal velocity along the fluid column at the maximal displacement,  $\rho_2/\rho_1 = 0.859$ ,  $h_2/h_1 = 1/5$ .

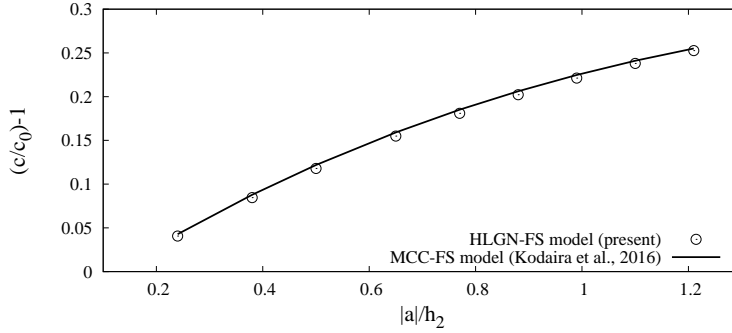


Figure 18: Excess propagation speed  $(c/c_0) - 1$  versus amplitude,  $\rho_2/\rho_1 = 0.859$ ,  $h_2/h_1 = 1/5$ .

surface disturbance is not observed in the present experiments. Further investigation is required to assess the existence of these surface disturbances.

The horizontal velocity along the fluid column at the maximal displacement is presented in Figure 21, where the MCC-FS results and the HLG-N-FS results are included. Some differences appear between the MCC-FS results and the HLG-N-FS results for this deep configuration case. For the upper-layer horizontal velocity, the horizontal velocity predicted by the MCC-FS model are larger than those obtained by the HLG-N-FS model. Meanwhile, for the lower-fluid layer near the maximal displacement, the horizontal velocity obtained by the MCC-FS model is larger than that obtained by the HLG-N-FS model. Near the bottom, the MCC-FS model predicts smaller horizontal velocity than that of the HLG-N-FS model.

Variations of the exceedance wave speed with the wave amplitude obtained by the HLG-N-FS model and the MCC-FS model are shown in Figure 22. The wave speed predicted by the MCC-FS model is slightly larger than that obtained by the HLG-N-FS model.

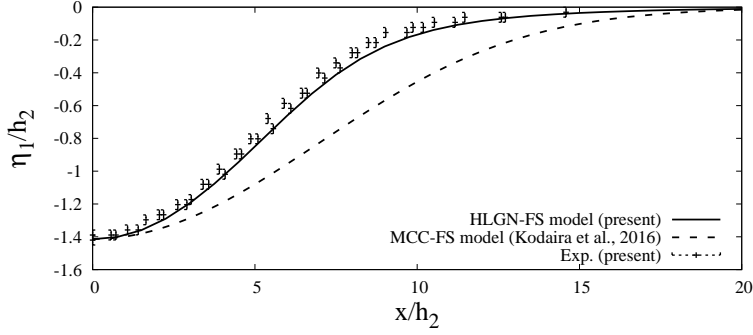
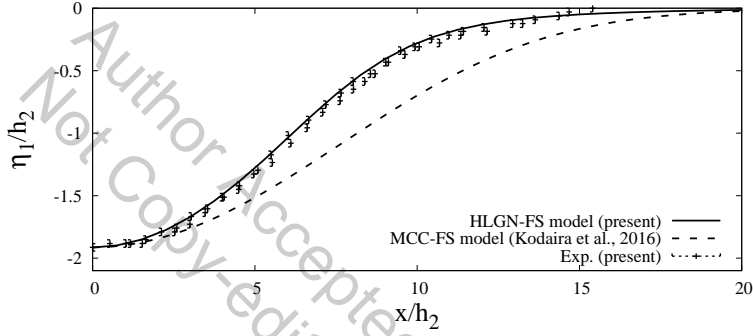
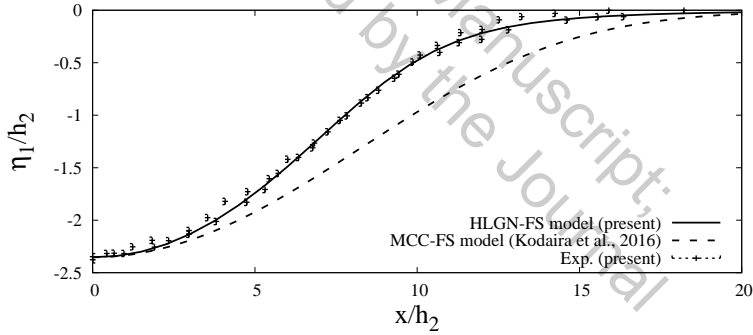
For this case, we find that the MCC-FS results do not agree well with the present experimental data. Meanwhile, the HLG-N-FS model is shown to be accurate to describe the internal solitary waves with a free surface in this case.

To further assess the differences between the HLG-N-FS and the MCC-FS results, the linear dispersion relation of the HLG-N-FS model with different levels is compared with the exact linear dispersion relation (Ten & Kashiwagi 2004), given as

$$K(k \sinh kh - K \cosh kh) + \varepsilon(K^2 - k^2) \sinh kh_1 \sinh kh_2 = 0, \quad (5.1)$$

where  $K = \omega^2/g$ ,  $h = h_1 + h_2$  and  $\varepsilon = 1 - (\rho_2/\rho_1)$ . The accuracy of the HLG-N-FS model with different levels is shown in Figure 23 for the case of  $\rho_2/\rho_1 = 0.869$  and  $h_2/h_1 = 1/15$ .

Also shown in Figure 23, is the accuracy of the linear dispersion relation of the MCC-FS model. The MCC-FS and the HLG-N-1-1-FS results are on top of each other, and they predict the wave speed well for waves with  $kh_1 < 3$ . It is observed that higher level of the HLG-N-FS model provides better agreement with the exact results for larger values of  $kh_1$ . The wave speed calculated by the HLG-N-5-5-FS model is within 2% error of the exact solution for waves with  $kh_1 < 20$ . Following the definition of half-amplitude point  $\lambda_{0.5}$  by Koop & Butler (1981), and based on the present experimental results, we estimate that for the cases of  $a/h_2 = -1.41, -1.91$  and  $-2.35$  in this subsection,  $kh_1$  is approximately 17, 14 and 13, respectively. Shown in Figure 23, the MCC-FS model

(a)  $a/h_2 = -1.41$ .(b)  $a/h_2 = -1.91$ .(c)  $a/h_2 = -2.35$ .Figure 19: Profiles of internal solitary waves,  $\rho_2/\rho_1 = 0.869$ ,  $h_2/h_1 = 1/15$ .

and the HLGN-1-1-FS model do not predict accurately these internal solitary waves for deep configurations. The high level HLGN-FS models, for example HLGN-5-5-FS model, predict accurately the internal solitary waves for both shallow and deep configurations.

## 6. Conclusions

In this study, large-amplitude internal solitary waves in a two-layer fluid system with a free surface are investigated by use of experimental and theoretical approaches. Laboratory experiments are conducted for some strongly nonlinear, deep-configuration,

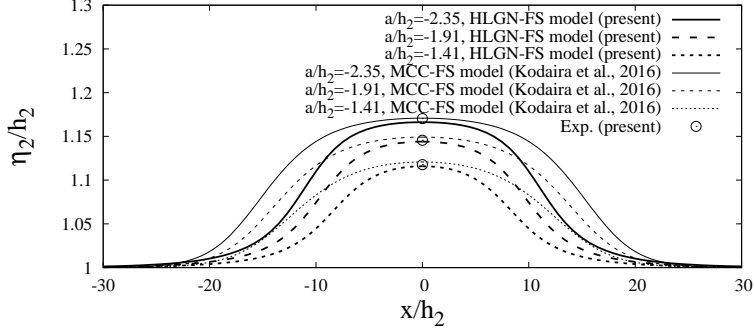


Figure 20: Wave profiles on the free surface.

internal solitary-wave cases. Upon comparison of existing numerical solution of the problem, including the MCC-FS model proposed by Kodaira *et al.* (2016), it was found that the existing numerical models do not provide accurate results under such conditions. This formed the motivation of developing a two-layer fluids model based on the High-Level Green-Naghdi equations, which can also include the free-surface effects, namely the HLG-N-FS model. Comparisons of the results of the HLG-N-FS model with the laboratory experiments show excellent agreement.

We apply the HLG-N-FS model to study the internal solitary waves for three cases, and consider the wave profile, velocity field and wave speed. The conclusions are as follows:

When the density ratio between the two fluids with constant densities is close to 1 (e.g.  $\rho_2/\rho_1 = 0.977$ , Case 1), the rigid-lid assumption is reasonable. When the density ratio between the two fluids is not close to 1 (e.g.  $\rho_2/\rho_1 = 0.859$ , Case 2;  $\rho_2/\rho_1 = 0.869$ , Case 3), the free-surface effects should be included;

For the strongly nonlinear, shallow-configuration case (e.g.  $\rho_2/\rho_1 = 0.859$  and  $h_2/h_1 = 1/5$ , Case 2), the HLG-N-FS model and the MCC-FS model both provide accurate solutions of the internal solitary waves with a free surface;

For the strongly nonlinear, deep-configuration case (e.g.  $\rho_2/\rho_1 = 0.869$  and  $h_2/h_1 = 1/15$ , Case 3), the HLG-N-FS results match the experimental data much better than those provided by the MCC-FS model. Thus, the HLG-N-FS model is shown to be accurate for describing the internal solitary waves for both shallow and deep configurations with free surface.

## Acknowledgement

The first and third authors' (BBZ and WYD) work is supported by the National Natural Science Foundation of China (No. 51490671, 11572093), International Science and Technology Cooperation Project sponsored by National Ministry of Science and Technology of China (No. 2012DFA70420) and the Special Fund for Basic Scientific Research of Central Colleges (Harbin Engineering University). The authors are grateful to the anonymous referees for their comments that improved our paper.



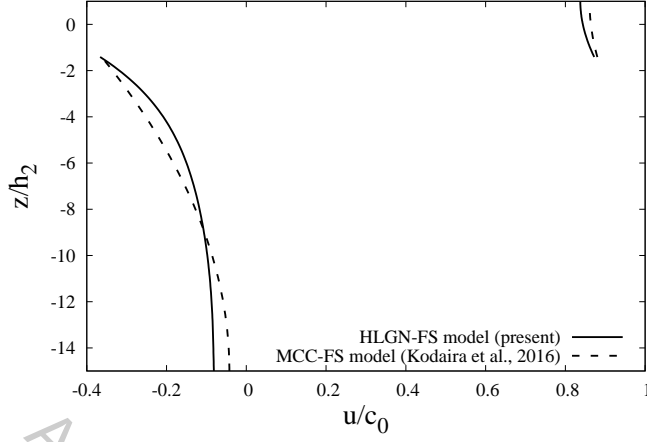
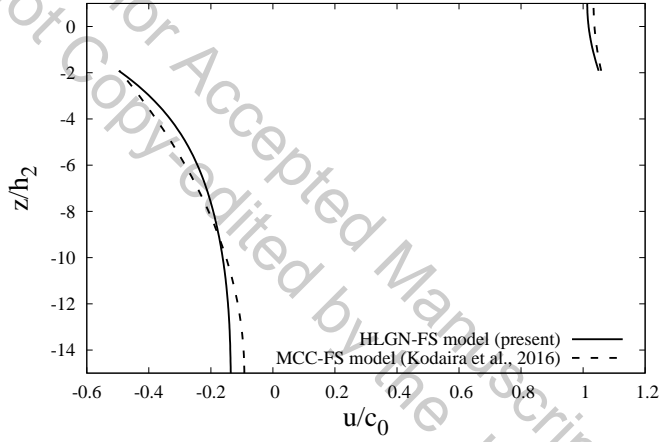
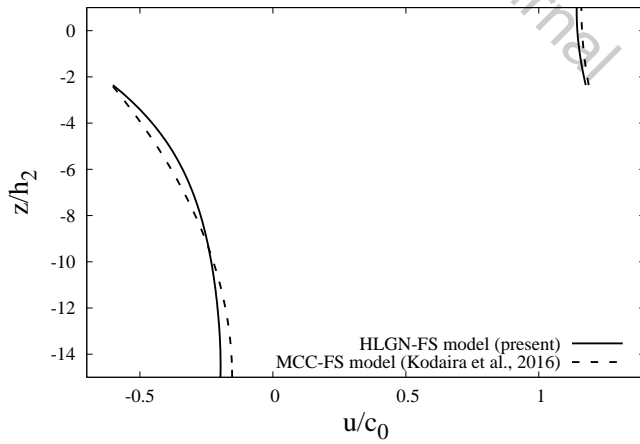
(a)  $a/h_2 = -1.41$ .(b)  $a/h_2 = -1.91$ .(c)  $a/h_2 = -2.35$ .

Figure 21: Horizontal velocity along the fluid column at the maximal displacement,  $\rho_2/\rho_1 = 0.869$ ,  $h_2/h_1 = 1/15$ .

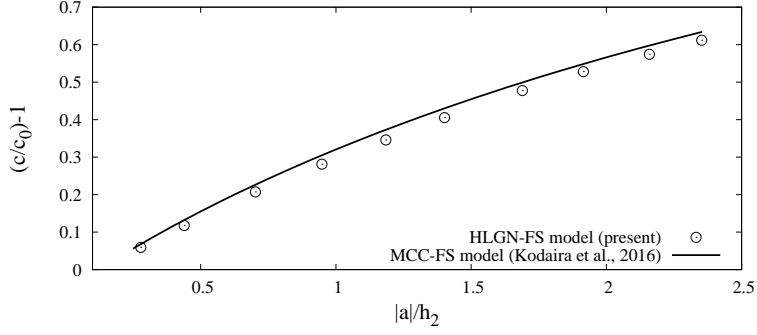


Figure 22: Excess propagation speed  $(c/c_0) - 1$  versus amplitude,  $\rho_2/\rho_1 = 0.869$ ,  $h_2/h_1 = 1/15$ .

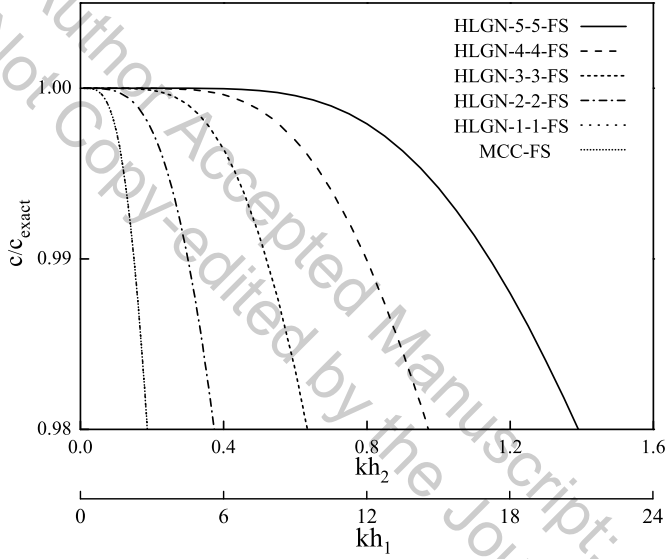


Figure 23: Accuracy of the linear dispersion relations of the HLGN-FS model and the MCC-FS model, compared with the exact linear dispersion relation (Ten & Kashiwagi 2004),  $\rho_2/\rho_1 = 0.869$ ,  $h_2/h_1 = 1/15$ . The MCC-FS and the HLGN-1-1-FS results are on top of each other.

## REFERENCES

- CAMASSA, R., CHOI, W., MICHALLET, H., RUSAS, P. & SVEEN, J. K. 2006 On the realm of validity of strongly nonlinear asymptotic approximations for internal waves. *Journal of Fluid Mechanics* **549**, 1–24.
- CARR, M., KING, S. E. & DRITSCHEL, D. G. 2011 Numerical simulation of shear-induced instabilities in internal solitary waves. *Journal of Fluid Mechanics* **683**, 263–288.
- CHOI, W. & CAMASSA, R. 1996 Weakly nonlinear internal waves in a two-layer system. *Journal of Fluid Mechanics* **313**, 83–103.
- CHOI, W. & CAMASSA, R. 1999 Fully nonlinear internal waves in a two-fluid system. *Journal of Fluid Mechanics* **396**, 1–36.
- DEBSARMA, S., DAS, K. P. & KIRBY, J. T. 2010 Fully nonlinear higher-order model equations for long internal waves in a two-fluid system. *Journal of Fluid Mechanics* **654** (1), 281–303.
- DUDA, T. F., LYNCH, J. F., IRISH, J. D., BEARDSLEY, R. C., RAMP, S. R., CHIU, C. S., Y., TANG T. & YANG, Y. 2004 Internal tide and nonlinear internal wave behavior at the continental slope in the northern south china sea. *IEEE Journal of Oceanic Engineering* **29** (4), 1105–1130.
- FORGIA, G. & SCIOTINO, G. 2019 The role of the free surface on interfacial solitary waves. *Physics of Fluids* **31**, 106601.
- FRUCTUS, D., CARR, M., GRUE, J., JENSEN, A. & DAVIES, P. A. 2009 Shear-induced breaking of large internal solitary waves. *Journal of Fluid Mechanics* **620**, 1–29.
- GRUE, J. 2006 Very large internal waves in the ocean - observations and nonlinear models. In *Waves in Geophysical Fluids*, pp. 205–270. Springer.
- GRUE, J., JENSEN, A., RUSAS, P.-O. & SVEEN, J. K. 1999 Properties of large-amplitude internal waves. *Journal of Fluid Mechanics* **380**, 257–278.
- HELFRICH, K. R. & MELVILLE, W. K. 2006 Long nonlinear internal waves. *Annual Review of Fluid Mechanics* **38**, 395–425.
- HUANG, X., CHEN, Z., ZHAO, W., ZHANG, Z., ZHOU, C., YANG, Q. & TIAN, J. 2016 An extreme internal solitary wave event observed in the northern South China Sea. *Scientific Reports* **6**, 30041.
- JO, T. & CHOI, W. 2008 On stabilizing the strongly nonlinear internal wave model. *Studies in Applied Mathematics* **120**, 65–85.
- KAO, T. W., PAN, F.-S. & RENOUEAU, D. 1985 Internal solitons on the pycnocline: generation, propagation, and shoaling and breaking over a slope. *Journal of Fluid Mechanics* **159**, 19–53.
- KODAIRA, T., WASEDA, T., MIYATA, M. & CHOI, W. 2016 Internal solitary waves in a two-fluid system with a free surface. *Journal of Fluid Mechanics* **804**, 201–223.
- KOOP, C. G. & BUTLER, G. 1981 An investigation of internal solitary waves in a two-fluid system. *Journal of Fluid Mechanics* **112**, 225–251.
- LAMB, H. 1932 In *Hydrodynamics*. Dover.
- LAMB, K. G. & FARMER, D. 2011 Instabilities in an internal solitary-like wave on the oregon shelf. *Journal of Physical Oceanography* **41** (1), 67–87.
- MICHALLET, H. & BARTHELEMY, E. 1997 Ultrasonic probes and data processing to study interfacial solitary waves. *Experiments in Fluids* **22**, 380–386.
- MICHALLET, H. & BARTHELEMY, E. 1998 Experimental study of interfacial solitary waves. *Journal of Fluid Mechanics* **366**, 159–177.
- MILES, J. W. 1980 Solitary waves. *Annual Review of Fluid Mechanics* **12** (1), 11–43.
- MIYATA, M. 1985 An internal solitary wave of large amplitude. *La Mer* **23**, 43–48.
- MIYATA, M. 1988 Long internal waves of large amplitude. In *Nonlinear Water Waves*, pp. 399–406. Springer.
- OSTROVSKY, L. A. & GRUE, J. 2003 Evolution equations for strongly nonlinear internal waves. *Physics of Fluids* **15** (10), 2934–2948.
- OSTROVSKY, L. A. & STEPANYANTS, Y. A. 2005 Internal solitons in laboratory experiments: Comparison with theoretical models. *Chaos* **15** (3), 037111.
- STANTON, T. P. & OSTROVSKY, L. A. 1998 Observations of highly nonlinear internal solitons over the continental shelf. *Geophysical Research Letters* **25** (14), 2695–2698.

- TEN, I. & KASHIWAGI, M. 2004 Hydrodynamics of a body floating in a two-layer fluid of finite depth. Part 1. Radiation problem. *Journal of Marine Science and Technology* **9**, 127–141.
- ZHAO, B. B., DUAN, W. Y. & ERTEKIN, R. C. 2014 Application of higher-level GN theory to some wave transformation problems. *Coastal Engineering* **83**, 177–189.
- ZHAO, B. B., ERTEKIN, R. C., DUAN, W. Y. & WEBSTER, W. C. 2016 New internal-wave model in a two-layer fluid. *Journal of Waterway, Port, Coastal and Ocean Engineering* **142** (3), 04015022.

Author Accepted Manuscript;  
Not Copy-edited by the Journal